Science Advances
AAAS

advances.sciencemag.org/cgi/content/full/7/1/eabc0467/DC1

Supplementary Materials for

Acoustofluidic centrifuge for nanoparticle enrichment and separation

Yuyang Gu, Chuyi Chen, Zhangming Mao, Hunter Bachman, Ryan Becker, Joseph Rufo, Zeyu Wang, Peiran Zhang, John Mai, Shujie Yang, Jinxin Zhang, Shuaiguo Zhao, Yingshi Ouyang, David T. W. Wong, Yoel Sadovsky, Tony Jun Huang*

*Corresponding author. Email: tony.huang@duke.edu

Published 1 January 2021, *Sci. Adv.* **7**, eabc0467 (2021)
DOI: 10.1126/sciadv.abc0467

The PDF file includes:

Other Supplementary Material for this manuscript includes the following:

(available at advances.sciencemag.org/cgi/content/full/7/1/eabc0467/DC1)

Note S1: Analysis of droplet spin

In our experimental configuration, a droplet is resting on a piezoelectric substrate and confined by a PDMS ring. Exciting the slanted IDTs causes two surface acoustic beams to propagate along the substrate and to enter the droplet. The acoustic radiation pressure created by these beams can induce both liquid-air interface deformation and vortex streaming inside the droplet. At this point, the droplet is subject to an increasing angular momentum and starts to spin about its vertical axis. With the spinning motion, the shape of the droplet evolves into a family of axisymmetric concave ellipsoid shapes. In the experiment, we found that the rotational velocity fits with the velocity of the normal mode (Raleigh) oscillation as shown in Eq. (1) (*33*). Although the rotational speed is primarily related to the radius, density, and surface tension of the droplet, the acoustic waves mainly induce inertial flow (i.e., the primary internal streaming and secondary azimuthal flow) which may influence the droplet shape and motion as well (*38*).

We investigated how different acoustic parameters (e.g., frequency, amplitude) may affect the droplet spinning motion as shown in Figure S(1)-(2). Analyzing the spinning droplet allows us to extract a radial waveform from a point on the spinning droplet for further analysis. As shown in Figure S1(c), the slanted IDTs can generate acoustic waves with different frequencies at different spatial locations. To verify this effect, we used a frequency sweep and extracted the resulting position waveform variation with time. Furthermore, we investigated varying the applied frequency and changes in the droplet shape *via* a wavelet transform of the positional waveform. The x-axis and y-axis show the time and frequency of the droplet spin, respectively, and the intensity of the wavelet map indicates the intensity of the waveform, which corresponds to the major axis length of the oblate ellipsoid droplet. It was found that with different acoustic wave frequencies, the droplet spinning frequency changed insignificantly, although there is a small fluctuation that may due to undesired turbulence. Meanwhile, at higher frequencies (9.5-11 MHz), it is found the wavelet intensity is stronger than at lower frequencies (7.5-9 MHz). This shows that at a higher frequency the droplet tends to get pulled apart and deform more

severely. At the same frequency, we also studied the influence of the acoustic amplitude, as shown in Figure S2. Notably, we found that with a slight increase in the acoustic amplitude within a small range, the droplet shape will slightly fluctuate and form a 4-lobed shape. As the angular momentum accumulates to a higher amplitude, the 4-lobed shaped droplet will gradually deform and transition into a 2-lobed shape. Meanwhile, the higher acoustic power will induce a stronger deformation in the droplet, which is indicated by the higher intensity of the wavelet transform. As indicated in Eq. (2), we can also obtain the radial and tangent velocity as:

$$\mathrm{v}_{drop-radial}(\varphi, \mathrm{t}) = \frac{\partial r(\varphi,t)}{\partial t} = \mathrm{a}[1 - \varepsilon_0 \sin(\omega_l t)\cos(\mathrm{l}\varphi + \varphi_0)] \quad \text{(S1)}$$

and

$$\mathrm{v}_{drop-tangent}(\varphi, \mathrm{t}) = \omega_l \mathrm{r}(\varphi, \mathrm{t}) \quad \text{(S2)}$$

which can be utilized to calculate the particle trajectory in combination with the vortex streaming.

As discussed above, with a relatively low acoustic excitation energy, the droplet can form a 4-lobed shape while rotating. We further investigated if other mode shapes could be excited by the acoustic waves. Experimentally, we observed that with larger droplet volumes, higher spinning modes can be generated at lower acoustic excitation amplitudes. As shown in Figure S3, 4-lobed and 6-lobed shapes are observed with droplet volumes of 30 μL and 60 μL, respectively. And, with a higher acoustic amplitude and a longer spin time, the droplet will eventually become a stable 2-lobed shape and keep spinning at the same velocity as the higher spin mode. The 2D droplet spinning motion and the corresponding velocity field and shear rate are simulated using Comsol Multiphysics 5.4 as described in Note S5.

Note S2: Vortex streaming and particle trajectory characterization

As the acoustic wave propagates into the droplet from its two flanks, bulk acoustic streaming is generated because of the closed volume of the droplet (*39*). Acoustic streaming is the time-averaged steady flow

that is created as a result of Reynolds stress, where a gradient in the momentum flux forces fluids to flow in association with a dissipation of acoustic energy flux. As the droplet spins, a single streaming vortex can be formed inside the droplet. The particle trajectory can be calculated *via* integration of the velocity, which combines the vortex streaming field and droplet spinning motion:

$$\mathrm{x}_{radial} = \int_0^t \mathrm{v}_{drop-radial} + \mathrm{v}_{vortex-radial} dt \quad \text{(S3)}$$

$$\mathrm{x}_{tangent} = \int_0^t \mathrm{v}_{drop-tangent} + \mathrm{v}_{vortex-tangent} dt \quad \text{(S4)}$$

The FEM-based software package, COMSOL Multiphysics 5.4 (the COMSOL group) is utilized to calculate the particle trajectory. The details are stated in Note S5.

Note S3: Drag force calculation

The common Stokes drag force $\mathrm{F}_H = 6\pi\eta r_p v$ is applicable for fluids with relatively low Reynolds numbers ($\mathrm{Re} < 1$) (*51*). In a single-droplet acoustofluidic centrifuge system, the fluid velocity is relatively large (in a rotating 30 μL droplet, the typical flow velocity is 40-80 mm/s), which yields a Reynolds number of $\mathrm{Re} = (\rho_\mathrm{f} v L)/\mu > 1$ (in a 30 μL droplet, Re is about 40, the maximum Re used in the experiments was ~135), where ρ_f, v, L, and μ are density of the fluid, flow velocity relative to the particle, characteristic linear dimension (droplet dimension), and dynamic viscosity, respectively.

Thus, we calculated the hydrodynamic force using the Schiller-Naumann model (*51*, *52*), which is applicable when $\mathrm{Re} > 1$:

$$F_H = \frac{3\mu C_D Re_r m_p}{4\rho_p {d_p}^2} v \quad \text{(S5)}$$

where $\mathrm{C}_D = \frac{24}{Re_r}(1 + 0.15{Re_r}^{0.687})$, $Re_r = \frac{\rho_f |v| d_p}{\mu}$, and ρ_p, d_p, m_p are density, diameter, and mass of the particle, respectively.

Note S4: Theory and numerical models of internal acoustic streaming

The internal acoustic streaming in the droplet confined by a PDMS ring are governed by equations (*53*, *54*)

$$\rho_0 \nabla \cdot \boldsymbol{v} = 0 \tag{S6}$$

$$\rho_0(\boldsymbol{v} \cdot \nabla)\boldsymbol{v} = -\nabla p + \mu \nabla^2 \boldsymbol{v} + \left(\mu_b + \frac{1}{3}\mu\right)\nabla(\nabla \cdot \boldsymbol{v}) + \boldsymbol{F} \tag{S7}$$

where the variables $\boldsymbol{v}$ and p are the streaming velocity and pressure in the liquid, and the parameters ρ_0, μ, and μ_b are the liquid density, shear viscosity, and bulk viscosity, respectively. The acoustic streaming is activated by a body force $\boldsymbol{F}$ induced by leaky SAW propagation which is relative to the acoustic particle velocity ($\boldsymbol{v_1}$) following (*53*, *54*)

$$F_x = -\rho_0 \left(\frac{\partial \overline{u_1 u_1}}{\partial x} + \frac{\partial \overline{v_1 u_1}}{\partial y} + \frac{\partial \overline{w_1 u_1}}{\partial z}\right) \tag{S8a}$$

$$F_y = -\rho_0 \left(\frac{\partial \overline{u_1 v_1}}{\partial x} + \frac{\partial \overline{v_1 v_1}}{\partial y} + \frac{\partial \overline{w_1 v_1}}{\partial z}\right) \tag{S8b}$$

$$F_z = -\rho_0 \left(\frac{\partial \overline{u_1 w_1}}{\partial x} + \frac{\partial \overline{v_1 w_1}}{\partial y} + \frac{\partial \overline{w_1 w_1}}{\partial z}\right) \tag{S8c}$$

The leaky SAW velocity of waves propagating in +y direction can be expressed by(*56*)

$$u_1 = 0 \tag{S9a}$$

$$v_1 = i\omega\left(A_m e^{i\omega t} e^{-ik_L y} e^{-\alpha k_L z}\right) \tag{S9b}$$

$$w_1 = i\omega\left(-i\alpha A_m e^{i\omega t} e^{-ik_L y} e^{-\alpha k_L z}\right) \tag{S9c}$$

where A_m is the amplitude of substrate vibration, k_L is the wave number of the leaky SAW, and α is the attenuation coefficient, respectively. By substituting Eqs. (S9) into Eqs. (S8), the streaming force can be express by

$$F_x = 0 \tag{S10c}$$

$$F_y = -(1 + \alpha_1^2) A_m^2 \omega^2 k_i e^{[2(k_i y + \alpha_1 k_i z)]} \tag{S10c}$$

$$F_z = -(1 + \alpha_1^2) A_m^2 \omega^2 k_i \alpha_1 e^{[2(k_i y + \alpha_1 k_i z)]} \tag{S10c}$$

in which $\alpha = i\alpha_1$.

The FEM-based software package, COMSOL Multiphysics 5.4 (the COMSOL group), was employed to numerically solve Eqs. (S6) and (S7) which govern the acoustic streaming in the droplet. A predefined "laminar flow" interface was used to solve the equations. The body force in Eqs. (S10) was applied by adding a "volume force" condition. The boundary conditions on the water-solid interfaces were set to "no slip" ($\boldsymbol{u} = \boldsymbol{0}$), which confines the velocity on the PDMS wall and substrate to be zero. And the boundary condition on the droplet-air interface was set to "slip" ($\boldsymbol{u} \cdot \boldsymbol{n} = 0$; $\boldsymbol{K_n} - (\boldsymbol{K_n} \cdot \boldsymbol{n})\boldsymbol{n} = \boldsymbol{0}$, where $\boldsymbol{K_n} = \mu(\nabla \boldsymbol{v} + (\nabla \boldsymbol{v})^T)\boldsymbol{n}$), which prescribes a no-penetration condition and assumes no viscous effects at the slip wall (*55*). The physics was solved *via* the COMSOL "stationary" solver. The value of some key parameters for the simulation are listed below.

Note S5: Numerical models of 2D particle trajectories in an acoustofluidic centrifuge

2D numerical models were solved using COMSOL Multiphysics 5.4(*55*) to investigate the flow field and particle movement on a horizontal cross-section (xy-plane) of the spinning droplet in an acoustofluidic centrifuge and to examine how the phenomenon responds to changes in parameters of interest (e.g., spin velocity, streaming velocity, shear rate, and particle size). The simulation domain was set to a quasi- ellipse with major semiaxis of R_a and minor semiaxis of R_b for droplets with deformation, or a circle with radius of R for droplets without deformation. The center of the domain was placed at spatial point (0, 0).

A predefined "Laminar Flow" interface was applied to the solution domain to solve the flow field in the domain governed by Eqs. (S6) and (S7). The "slip" ($\boldsymbol{u} \cdot \boldsymbol{n} = 0$) boundary, which confines the normal component of the velocity on the boundary to be zero, was applied to the profile of the quasi-ellipse (droplet-air interface). A "Volume Force" condition was added to apply the streaming force generated by two leaky SAW beams propagating in the +y and -y direction into the two flanks of the droplet. The

streaming force follows the expression in Eq. (S11a) and Eq. (S11b) for +y and -y SAW propagation, respectively:

$$F_y = -(1+\alpha_1^2)A_m^2\omega^2 k_i e^{2k_i y} \quad \text{(S11a)}$$

$$F_y = (1+\alpha_1^2)A_m^2\omega^2 k_i e^{2k_i(R_a-y)} \quad \text{(S11b)}$$

where A_m is the amplitude of substrate vibration, k_L is the wave number of the leaky SAW, and α is the attenuation coefficient, respectively. The spin motion of the droplet was modelled by applying a "Rotating Domain" condition (under "Moving Mesh" interface). The simulation domain was defined to rotate at a constant speed of f_r revolutions per second. The value of f_r was set within the range of 0-55 according to the experimentally measured value in each single case. The "Laminar Flow" and the "Rotating Domain" interfaces were solved together in the time domain to simulate the flow filed induced by leaky-SAWs propagation and spin of the droplet.

A "particle tracing for fluid flow" interface was applied to follow particle motion in the spinning droplet under the forces that might arise. The density and diameter of the particles were set in the "Particle properties" condition. The density of the PS particles was set to 1,050 kg/m^3 and the diameter of the particles was set to either 28 nm, 100 nm, or 1 μm. The particles were released either randomly using a "Release" condition with setting the number of particles, or regularly using a "Release from Grid" condition with defining the initial coordinates of the particles. The velocity of the particles ($\boldsymbol{v}$) induced by external forces ($\boldsymbol{F_t}$) was governed by the equation $\frac{d(m_p \boldsymbol{v})}{dt} = \boldsymbol{F_t}$. The forces were applied to the particles suspended in the fluid domain. In this case, we mainly considered two external forces, which are the acoustic radiation force and secondary-flow drag force. A "Drag Force" condition was added to apply the component of drag force induced by the flow velocity induced by leaky-SAW propagation and spin of the droplet ($\boldsymbol{u}$). The drag force follows the expression in Note S3. Since the acoustic radiation force and another component of drag force induced by droplet compression and expansion directed towards the center of the domain, a "Force" condition was applied to represent the combined effect of

these radial force components. The value of this radial force was adjusted in the ranged from 0 N to 10^{-10} N for different cases. These physical systems were solved using a time-dependent solver simultaneously with a step of 0.0001 s for 1 µm particles, and 0.000005 s for 28 nm and 100 nm particles. The detailed parameters used in the simulation are listed in the Table S4.

Supplementary Figures.

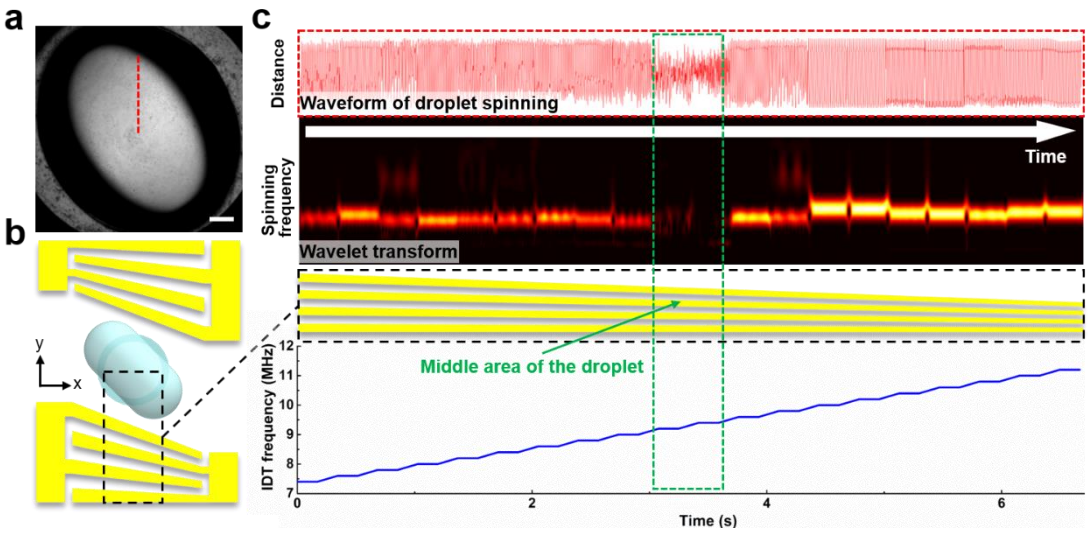

Figure S1: The influence of the acoustic frequency on the droplet spin speed in an acoustofluidic centrifuge. (a) The top view of the rotating droplet captured under a microscope. (b) Schematic of the experiment setup, where the slanted IDTs were excited with different frequencies corresponding to different spatial locations along the width of the black frame. (c) From top to bottom: the extracted waveform; the wavelet transforms of the waveform; the enlarged slanted IDT area; and, a plot of the excitation frequency versus time. The results show that frequency tuning has little influence on the droplet spin speed, except when the acoustic wave propagates into the droplet along the central area of the droplet. When the SAW enters the center of the droplet, very little rotation was observed due to a lack of rotational inertia being imparted into the flanks of the droplet.

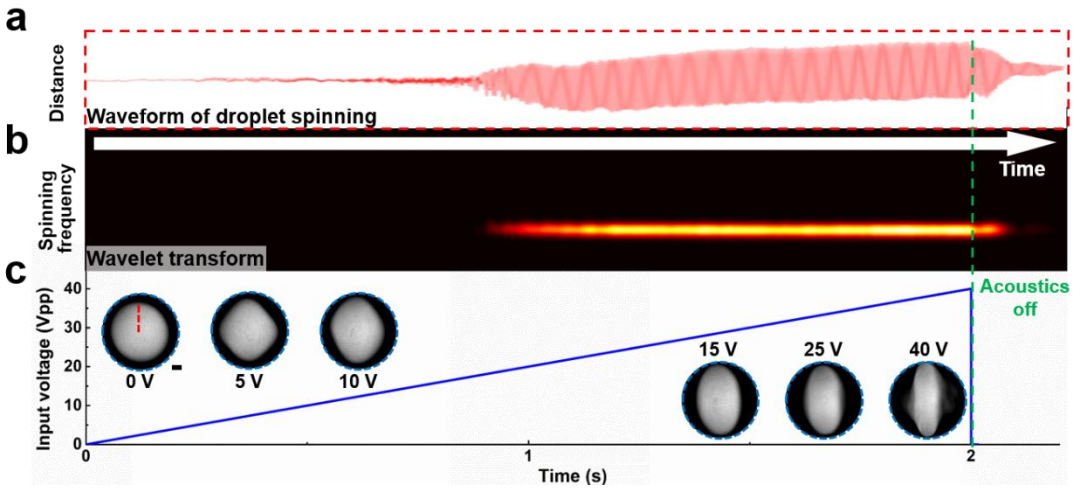

Figure S2: The influence of the acoustic power on droplet spin in an acoustofluidic centrifuge. The frequency is set to be 11 MHz, the excitation Vpp is tuned from 0 V to 40 V. (a) The waveform extracted from the spinning droplet. (b) The wavelet transforms with respect to changes in time. (c) Plot showing how the input voltage was varied as a function of time. At different voltages, the droplet starts to rotate from its equilibrium state and forms multiple lobes. As the voltage increased, both the acoustic radiation pressure and the centrifugal force increases, and the droplet gradually becomes a 2 lobed shape while maintaining its spin. Although there is a gradual shape change as the droplet starts to spin, the rotational velocity remains constant.

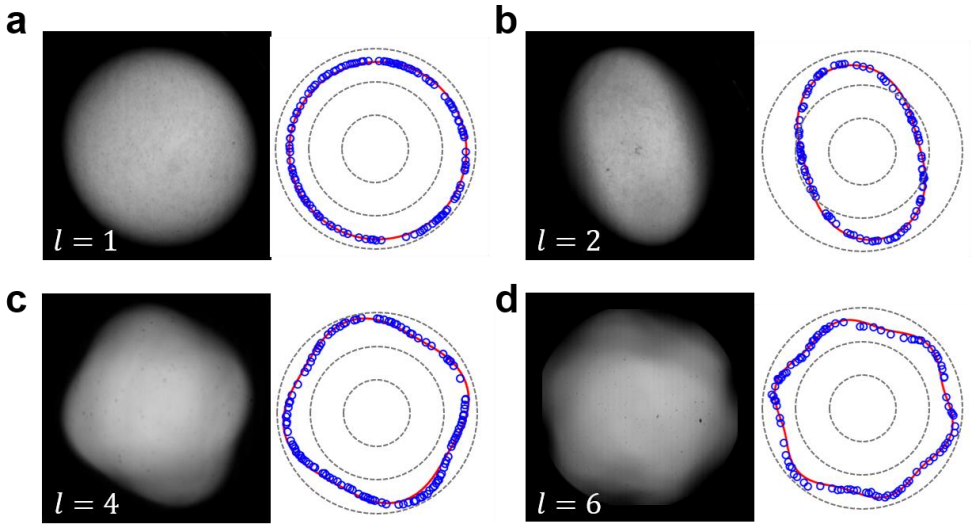

Figure S3: Photos (left) and outline comparisons (right) between the droplet (blue circle) and a fitted line (red line) for different droplet spin modes in an acoustofluidic centrifuge. (a) The initial equilibrium shape, (b) 2-lobed shape, (c) 4-lobed shape, and (d) 6-lobed shape, respectively. Red lines show the theoretical calculated outline, and blue circles indicate the experimental results extracted *via* image processing.

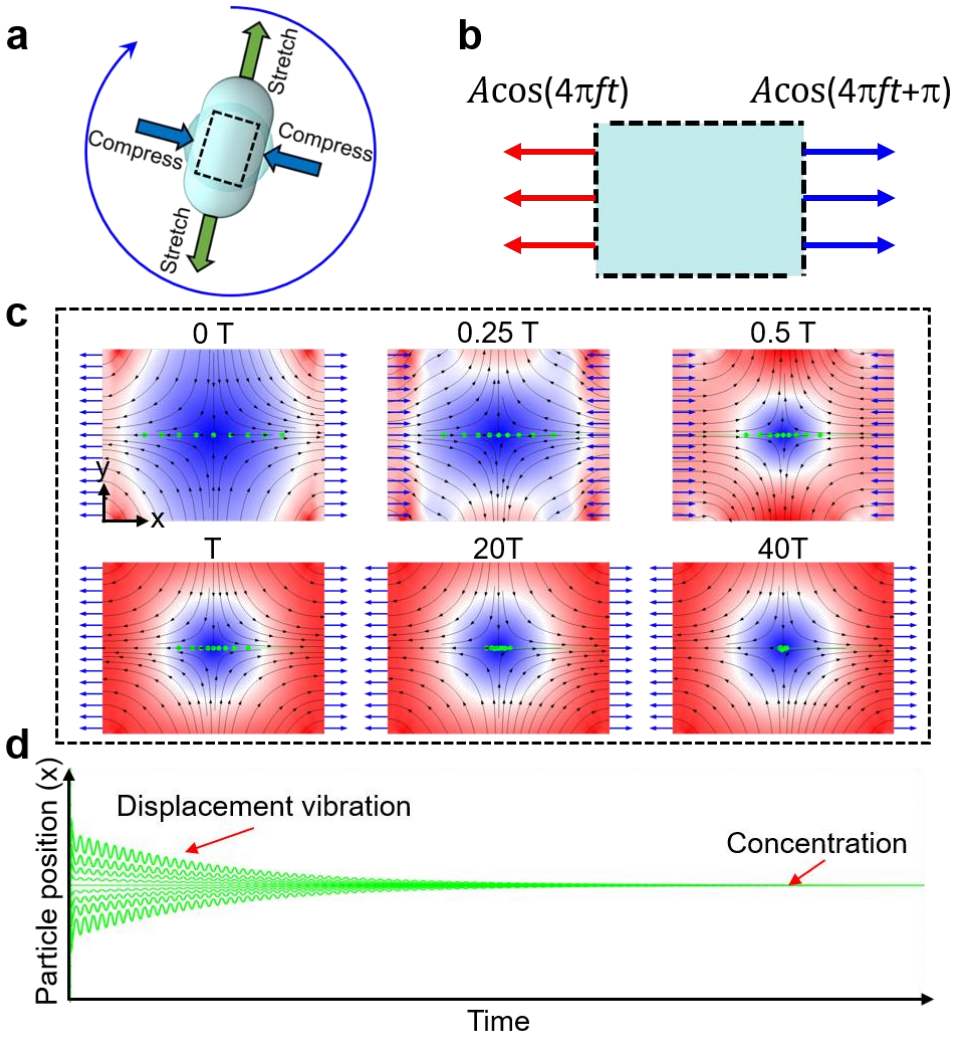

Figure S4: Simulation result showing the particle concentration due to the droplet spin and periodic boundary deformation. (a) Schematic of the droplet deformation during spin motion. (b) Boundary condition used for the simplified model simulation. A fluid region in the droplet is simulated with velocity profile added to two sides of the region (*i.e.,* "velocity" boundary condition). On both sides, the normal outflow velocity is set to be periodic (*i.e.,* $Acos(4\pi ft)$, where A is the velocity amplitude of the periodic deformation, f is the spin frequency which is the half of the deformation cycle along the radial direction) and inverted in order to simulate the flow field during the continuous compression and stretching. The other two sides are set as the "no pressure" boundary condition. (c) The particle motion under different time frames; with certain spinning cycles, the particles will be focused to the middle of

the droplet. (d) Particle position along the x-axis (aligned with the velocity direction) changes as the time varies. With a small displacement vibration, particles are gradually concentrated to the middle region.

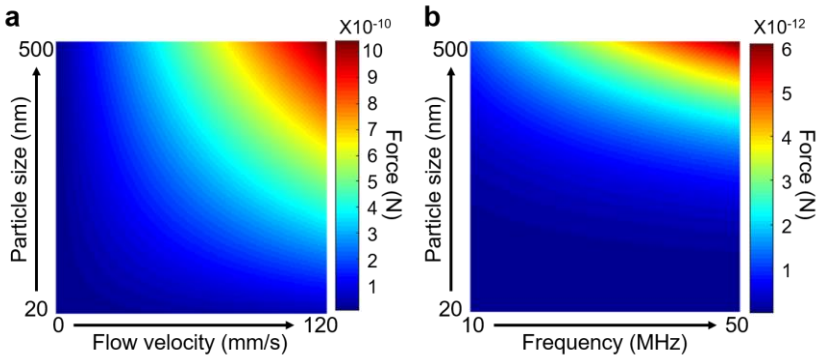

Figure S5: Factors that influence the particle motion within the spinning droplet in an acoustofluidic centrifuge. (a) Plot of the drag force effect (combined flow velocity) on the nanoparticles with different particle sizes and flow velocities. (b) Plot of the acoustic radiation force that acts on the nanoparticles with different particle sizes and frequencies.

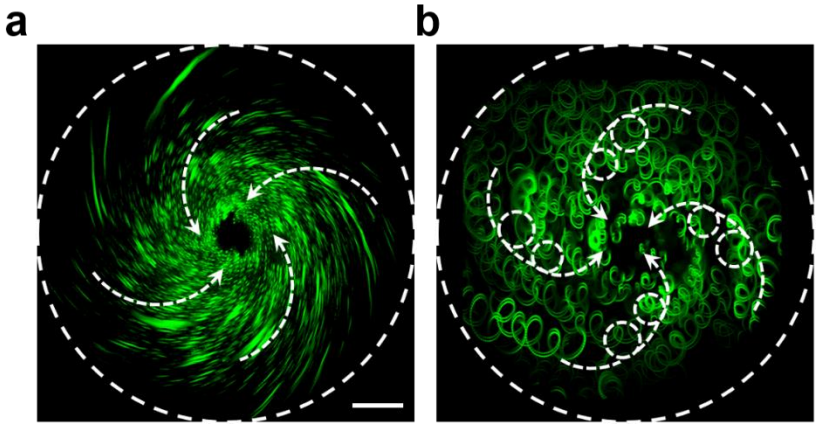

Figure S6: Experimentally observed particle trajectories within the droplet in an acoustofluidic centrifuge. Particle trajectories (a) without rotational motion of the droplet where particle motion is due to a small input voltage, and (b) within a stable spinning droplet.

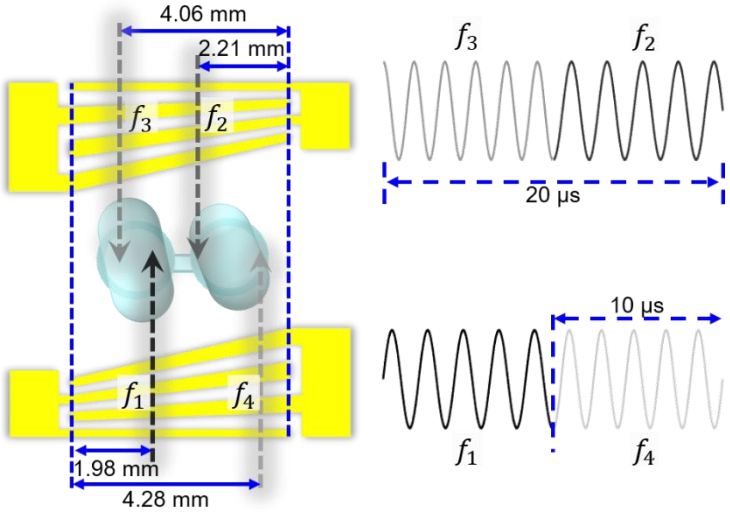

Figure S7: Dual-droplet acoustofluidic centrifuge. Acoustic beams with different frequencies are generated from different positions along the slanted IDTs (left). The orientation of the beams were chosen so that the beams would enter the droplets off the center axis and cause spinning. In order to generate two beams using a single IDT, frequency shift keying is used to repeatedly alternate between excitation signals (f_1 and f_4 for example) at a frequency of 100 kHz, corresponding to a 10 µs time window for each excitation period (right).

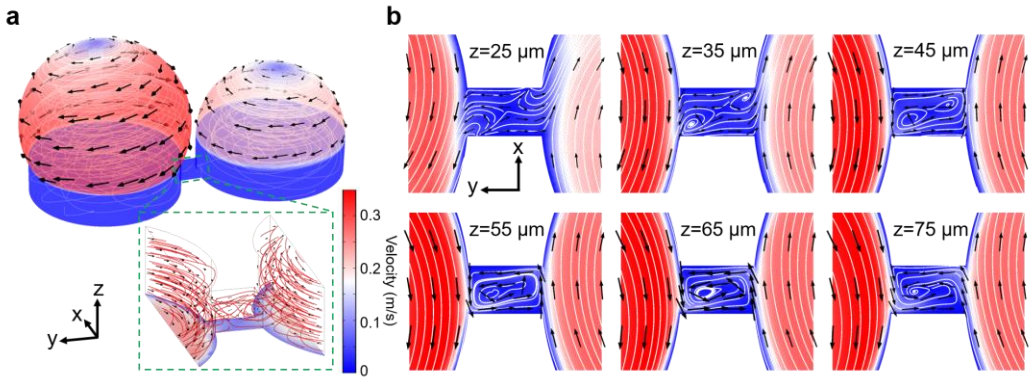

Figure S8: 3D flow field in a dual-droplet acoustofluidic centrifuge system. (a) The simulated 3D flow field in the dual-droplet system. (b) The flow fields at different z-planes in the microchannel. Details about the governing equations and the simulation model setup can be found in Supplementary Note S3.

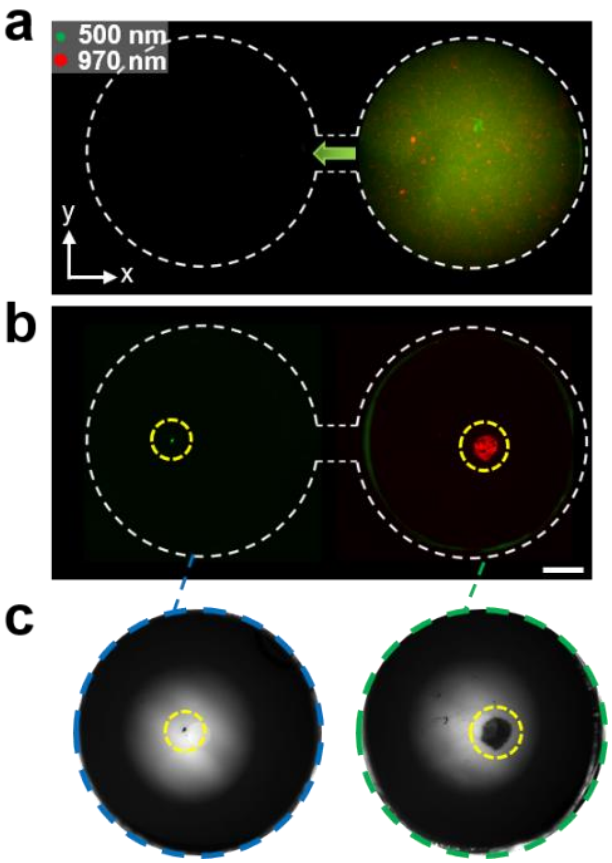

Figure S9: The separation and enrichment of particles with diameters of 500 nm and 970 nm *via* a dual-droplet acoustofluidic centrifuge. (a) Image showing the initial state before the acoustic field is turned on. The right droplet contains the particle samples and the left droplet is initially blank. (b) Image after the acoustic field is turned on; 500 nm particles are separated and transferred to the left droplet, and the 970 nm particles remain in the right droplet. After size-based separation, the respective particles are enriched in both droplets. Scale bar: 500 μm. (c) Bright-field image of the separated and enriched particles within the respective droplets. Both the left and right droplets show particle clusters at their centers.

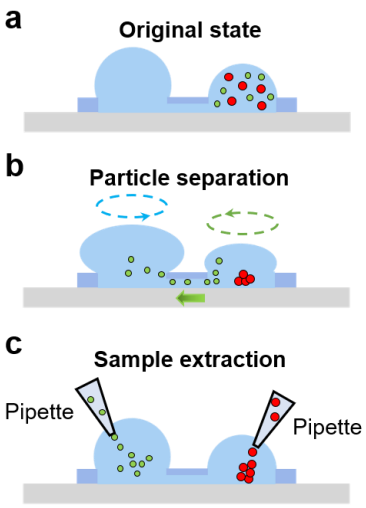

Figure S10: Schematic of the procedure of the particle transport and separation in dual-droplet acoustofluidic centrifuge. (a) The original system state contains one droplet (right) with the sample and one blank droplet (left). (b) With acoustic waves exciting, larger particles (red) are concentrated to the middle of the right droplet and the small particles (green) are gradually transferred to the left droplet. (c) After the separation and transport process, particles with different sizes are immersed in different droplets. Then two pipettes are used to extract the sample from droplets, respectively.

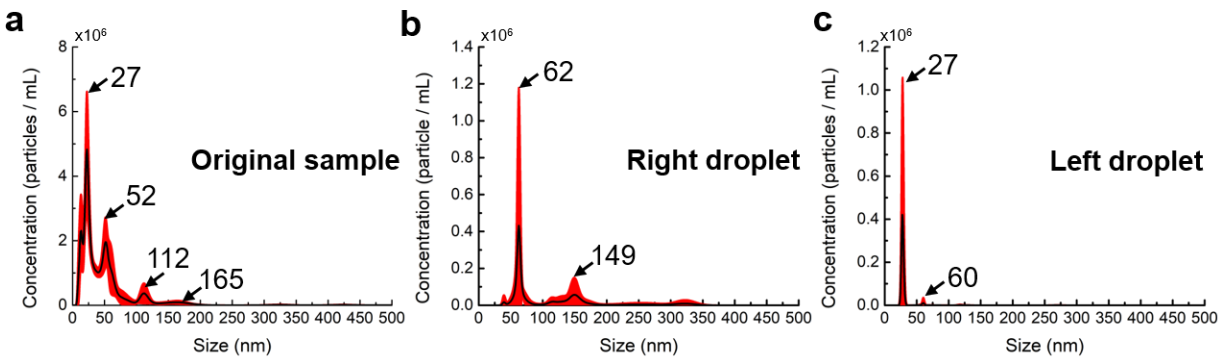

Figure S11: The NTA measurement of the exosome sample size distribution with 200 nm gate for (a) original sample, (b) post-process sample in right droplet, and (c) post-process sample in left droplet. The exosome sample was filtered through a 200 nm filter before the processing in the acoustofluidic centrifuge system.

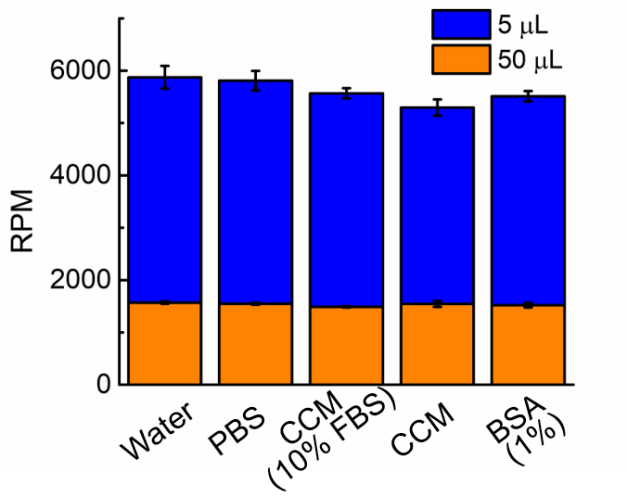

Figure S12: Droplet spinning speeds achieved with different organic liquids. Two different volumes were tested with a droplet radius of 1.1 mm for 5 μL and 2.5 mm for 50 μL. Purified water (as a control), PBS, cell culture medium (CCM) with 10% fetal bovine serum (FBS), cell culture medium, and Bovine Serum Albumin (BSA) solutions were tested as the five examples.

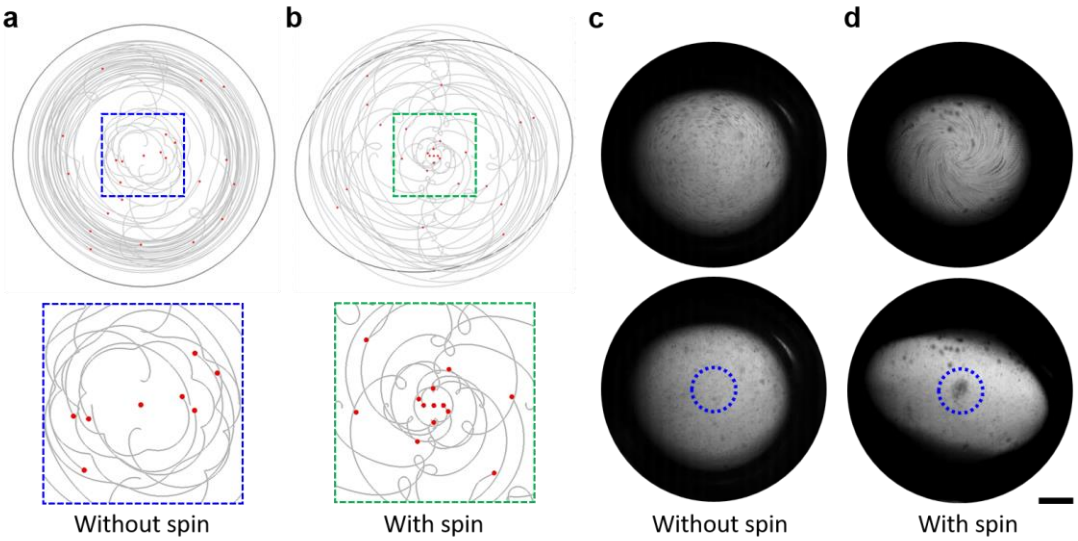

Figure S13: Particle motion comparison between non-spinning and spinning droplets. (a, b) Simulated particle trajectory (a) without and (b) with droplet spin. Particle trajectory shows stronger motion towards the droplet center when spinning. (c, d) Experimental particle trajectory (top) and status at 1 second (bottom) for the (c) without and (d) with droplet spinning conditions. Since droplet spin motion is driven by acoustic power, slight power differences are used for without (~5 Vpp) and with (~8 Vpp) droplet spin.

Table S1: Force characterization for particle motion in a spinning droplet.

Force	Force magnitude (N)*	Force direction	Formula(*51*, *52*, *56*, *57*)
Drag force (vortex streaming)	~0-10^{-10}	Tangential	$\boldsymbol{F}_H = \frac{3\mu C_D Re_r m_p}{4\rho_p {d_p}^2}\boldsymbol{v_T}$
Secondary-flow drag force (droplet deformation)	~0-10^{-11}	Radial	$\boldsymbol{F}_H = \frac{3\mu C_D Re_r m_p}{4\rho_p {d_p}^2}\boldsymbol{v}_R$ $\boldsymbol{v}_R = \frac{\boldsymbol{dR}_{droplet}}{\boldsymbol{dt}}$ $\boldsymbol{R}_{droplet} = (R_{max} - R_{min})\sin(2\pi(2f_{spin})t) + R_{min}$
Pressure gradient force (tangential)	~0-10^{-17}	Tangential	$\boldsymbol{F}_p = \frac{1}{6}\pi d_p^3 \rho \frac{D\boldsymbol{u_T}}{Dt}$
Pressure gradient force (radial)	~0-10^{-17}	Radial	$\boldsymbol{F}_p = \frac{1}{6}\pi d_p^3 \rho \frac{D\boldsymbol{u_R}}{Dt}$
Acoustic radiation force	~0-10^{-15}	Partially radial	$\boldsymbol{F}_{rad} = -\nabla\{V_p[\frac{f_1}{2\rho_0 {c_0}^2} < {p_1}^2 > - \frac{3\rho_0 f_2}{4} < \boldsymbol{v_1}\cdot\boldsymbol{v_1} >]\}$

* The forces are calculated for 100 nm particle in a 10 μL droplet (1.29 mm radius and 55 fps spin speed). Acoustic radiation force is calculated with 21.7 MHz, 300-800 kPa pressure amplitude.

Table S2: Exosome subpopulation distribution count and percentage of the pre- and post-separation samples for each trial.

	Trial number	90-150 nm (count)	60-80 nm (count)	~35 nm (count)	Total	90-150 nm (percent)	60-80 nm (percent)	~35 nm (percent)
Original	**#1**	9	8	13	30	0.30	0.27	0.43
	#2	6	5	18	29	0.21	0.17	0.62
	#3	4	12	13	29	0.14	0.41	0.45
	#4	2	2	9	13	0.15	0.15	0.69
	#5	3	12	8	23	0.13	0.52	0.35
					Average:	0.186	0.304	0.508
					STD:	0.071	0.159	0.141
Left droplet (post-separation)	**#1**	10	7	4	21	0.48	0.33	0.19
	#2	9	13	5	27	0.33	0.48	0.18
	#3	6	8	3	17	0.35	0.47	0.18
	#4	4	12	2	18	0.22	0.67	0.11
	#5	5	12	2	19	0.26	0.63	0.10
					Average:	0.328	0.516	0.152
					STD:	0.100	0.137	0.043
Right droplet (post-separation)	**#1**	0	2	10	12	0.00	0.17	0.83
	#2	0	2	7	9	0.00	0.22	0.78
	#3	1	2	14	17	0.06	0.12	0.82
	#4	0	2	7	9	0.00	0.22	0.78
	#5	0	0	9	9	0.00	0.00	1.00
					Average:	0.012	0.146	0.842
					STD:	0.027	0.091	0.091

Table S3: Comparison of different nanoparticle/exosome separation techniques

Techniques	Yields (%)	Purity (%)	Throughput	Unbiased isolation	Ability to separate exosome subpopulations	Advantages	Disadvantages
Differential Ultracentrifugation (*49*, *58*, *59*)	5-25	~33	~8 h	Yes	Limited	Large processing sample volume, Unbiased separation	Expensive equipment, relatively low yield
Polymer-assisted precipitation (*49*, *60*, *61*)	~40	~40	~12 h	Yes	Limited	Unbiased separation	Multiple procedures needed, long processing time
Immunoaffinity-based capture beads (*48*, *49*, *62*, *63*)	3-12	~60	18-24 h	No	Limited	Ability to separate disease-related exosomes	Long sample preparation time, additional washing process needed, biased separation
Immunoaffinity-based microfluidic chips (*48*, *49*, *64*, *65*)	7-33	~68	~2 h	No	Limited	Ability to separate disease-related exosomes	Additional washing process needed, biased separation
Field flow fractionation (*44*, *48*, *49*)	5-25	~33	~10 h	Yes	Yes	High separation resolution, ability to separate exosome sub-populations	Multiple procedures, Specific membrane required
Acoustofluidic centrifuge	80-86	82-96	~35 seconds	Yes	Yes	Ability to separate exosome sub-populations, high speed, high yield, high purity, simple configuration	Low sample volume per assay, potential evaporation issue

Table S4: Detailed parameters for numerical simulations.

Parameter	Symbol	Value
Density of the liquid	ρ_0	997 kg/m^3
Shear viscosity of the liquid	μ	1×10^{-3} Pa·s
Amplitude of substrate vibration	A_m	1.5 nm
Frequency of the SAW beams	f	13 MHz, 21.7 MHz
Major semiaxis of the elliptical droplet	R_a	1.5 mm
Minor semiaxis of the elliptical droplet	R_b	1.2 mm
Radius of the circular droplet domain	R	1.29 mm
Rotational velocity of the droplet	f_r	0-55 1/s
Density of the PS particles	ρ_p	1050 kg/m^3
Diameter of the PS particles	d_p	28 nm, 100 nm, 1 μm
Amplitude of the radial force	F_m	$0\text{-}1\times10^{-10}$ N

Supplementary Movies.

Movie S1. Droplet spinning motion under two viewpoints. This video was captured at 240 fps and replayed at 30 fps.

Movie S2. Top-view droplet spin observed under microscope. This video was captured at 3000 fps and replayed at 120 fps.

Movie S3. Particle trajectory tracking under the fluorescence microscope. This video was captured at 3,000 fps and replayed at 120 fps.

Movie S4. Fluorescent images showing the concentration of 28 nm polystyrene particles in a spinning droplet. This video is in real-time.

Movie S5. Fluorescent images showing the concentration of DNA molecules in a spinning droplet. This video was captured at 30 fps and replayed at 120 fps.

Movie S6. Simulation results showing the helical shaped particle trajectory in a spinning droplet.

Movie S7. Simulation results showing different particle trajectories and corresponding separation phenomenon. Particle color: Blue 28 nm, Red: 100 nm.

Movie S8. Top-view dual droplet spinning. This video was captured at 3000 fps and replayed at 60 fps.

Movie S9. Zoomed-in view of the microchannel between two spinning droplets. Particles with green fluorescence will transport from right droplet to left droplet. This video is in real-time.

REFERENCES AND NOTES

1. H. Lee, A. K. R. Lytton-Jean, Y. Chen, K. T. Love, A. I. Park, E. D. Karagiannis, A. Sehgal, W. Querbes, C. S. Zurenko, M. Jayaraman, C. G. Peng, K. Charisse, A. Borodovsky, M. Manoharan, J. S. Donahoe, J. Truelove, M. Nahrendorf, R. Langer, D. G. Anderson, Molecularly self-assembled nucleic acid nanoparticles for targeted *in vivo* siRNA delivery. *Nat. Nanotechnol.* **7**, 389–393 (2012).
2. C. M. H. Newman, T. Bettinger, Gene therapy progress and prospects: Ultrasound for gene transfer. *Gene Ther.* **14**, 465–475 (2007).
3. Y.-H. Lee, C.-A. Peng, Enhanced retroviral gene delivery in ultrasonic standing wave fields. *Gene Ther.* **12**, 625–633 (2005).
4. J. Sun, Y. Xianyu, X. Jiang, Point-of-care biochemical assays using gold nanoparticle-implemented microfluidics. *Chem. Soc. Rev.* **43**, 6239–6253 (2014).
5. X. Zhu, J. Wu, W. Shan, W. Tao, L. Zhao, J.-M. Lim, M. D'Ortenzio, R. Karnik, Y. Huang, J. Shi, O. C. Farokhzad, Polymeric nanoparticles amenable to simultaneous installation of exterior targeting and interior therapeutic proteins. *Angew. Chemie Int. Ed. Engl.* **55**, 3309–3312 (2016).
6. X. Huang, M. A. El-Sayed, Gold nanoparticles: Optical properties and implementations in cancer diagnosis and photothermal therapy. *J. Adv. Res.* **1**, 13–28 (2010).
7. K. Fan, C. Cao, Y. Pan, D. Lu, D. Yang, J. Feng, L. Song, M. Liang, X. Yan, Magnetoferritin nanoparticles for targeting and visualizing tumour tissues. *Nat. Nanotechnol.* **7**, 459–464 (2012).
8. M. A. Nash, J. N. Waitumbi, A. S. Hoffman, P. Yager, P. S. Stayton, Multiplexed enrichment and detection of malarial biomarkers using a stimuli-responsive iron oxide and gold nanoparticle reagent system. *ACS Nano* **6**, 6776–6785 (2012).
9. M. Stratakis, H. Garcia, Catalysis by supported gold nanoparticles: Beyond aerobic oxidative processes. *Chem. Rev.* **112**, 4469–4506 (2012).
10. G. Prieto, J. Zečević, H. Friedrich, K. P. de Jong, P. E. de Jongh, Towards stable catalysts by controlling collective properties of supported metal nanoparticles. *Nat. Mater.* **12**, 34–39 (2013).

11. H. Zhao, S. Sen, T. Udayabhaskararao, M. Sawczyk, K. Kučanda, D. Manna, P. K. Kundu, J.-W. Lee, P. Král, R. Klajn, Reversible trapping and reaction acceleration within dynamically self-assembling nanoflasks. *Nat. Nanotechnol.* **11**, 82–88 (2016).
12. A. Bekdemir, F. Stellacci, A centrifugation-based physicochemical characterization method for the interaction between proteins and nanoparticles. *Nat. Commun.* **7**, 13121 (2016).
13. S. Liu, T. D. Yuzvinsky, H. Schmidt, Effect of fabrication-dependent shape and composition of solid-state nanopores on single nanoparticle detection. *ACS Nano* **7**, 5621–5627 (2013).
14. J. Xu, K. J. Kwak, J. L. Lee, G. Agarwal, Lifting and sorting of charged Au nanoparticles by electrostatic forces in atomic force microscopy. *Small* **6**, 2105–2108 (2010).
15. A. Kunze, P. Tseng, C. Godzich, C. Murray, A. Caputo, F. E. Schweizer, D. Di Carlo, Engineering cortical neuron polarity with nanomagnets on a chip. *ACS Nano* **9**, 3664–3676 (2015).
16. A. H. J. Yang, S. D. Moore, B. S. Schmidt, M. Klug, M. Lipson, D. Erickson, Optical manipulation of nanoparticles and biomolecules in sub-wavelength slot waveguides. *Nature* **457**, 71–75 (2009).
17. B. J. Roxworthy, K. D. Ko, A. Kumar, K. H. Fung, E. K. C. Chow, G. L. Liu, N. X. Fang, K. C. Toussaint Jr., Application of plasmonic bowtie nanoantenna arrays for optical trapping, stacking, and sorting. *Nano Lett.* **12**, 796–801 (2012).
18. A. Ozcelik, J. Rufo, F. Guo, Y. Gu, P. Li, J. Lata, T. J. Huang, Acoustic tweezers for the life sciences. *Nat. Methods* **15**, 1021–1028 (2018).
19. K. Melde, A. G. Mark, T. Qiu, P. Fischer, Holograms for acoustics. *Nature* **537**, 518–522 (2016).
20. P. Li, Z. Mao, Z. Peng, L. Zhou, Y. Chen, P.-H. Huang, C. I. Truica, J. J. Drabick, W. S. El-Deiry, M. Dao, S. Suresh, T. J. Huang, Acoustic separation of circulating tumor cells. *Proc. Natl. Acad. Sci. U.S.A.* **112**, 4970–4975 (2015).
21. D. J. Collins, Z. Ma, Y. Ai, Highly localized acoustic streaming and size-selective submicrometer particle concentration using high frequency microscale focused acoustic fields. *Anal. Chem.* **88**, 5513–5522 (2016).
22. D. J. Collins, C. Devendran, Z. Ma, J. W. Ng, A. Neild, Y. Ai, Acoustic tweezers via sub–time-of-flight regime surface acoustic waves. *Sci. Adv.* **2**, ae1600089 (2016).

23. J. P. K. Armstrong, J. L. Puetzer, A. Serio, A. G. Guex, M. Kapnisi, A. Breant, Y. Zong, V. Assal, S. C. Skaalure, O. King, T. Murty, C. Meinert, A. C. Franklin, P. G. Bassindale, M. K. Nichols, C. M. Terracciano, D. W. Hutmacher, B. W. Drinkwater, T. J. Klein, A. W. Perriman, M. M. Stevens, Engineering anisotropic muscle tissue using acoustic cell patterning. *Adv. Mater.* **30**, 1802649 (2018).
24. M. V. Patel, A. R. Tovar, A. P. Lee, Lateral cavity acoustic transducer as an on-chip cell/particle microfluidic switch. *Lab Chip* **12**, 139–145 (2012).
25. R. Barnkob, P. Augustsson, T. Laurell, H. Bruus, Acoustic radiation-and streaming-induced microparticle velocities determined by microparticle image velocimetry in an ultrasound symmetry plane. *Phys. Rev. E.* **86**, 56307 (2012).
26. H. Li, J. R. Friend, L. Y. Yeo, Surface acoustic wave concentration of particle and bioparticle suspensions. *Biomed. Microdevices* **9**, 647–656 (2007).
27. M. Wu, Z. Mao, K. Chen, H. Bachman, Y. Chen, J. Rufo, L. Ren, P. Li, L. Wang, T. J. Huang, Acoustic separation of nanoparticles in continuous flow. *Adv. Funct. Mater.* **27**, 1606039 (2017).
28. M. S. Limaye, J. J. Hawkes, W. T. Coakley, Ultrasonic standing wave removal of microorganisms from suspension in small batch systems. *J. Microbiol. Methods* **27**, 211–220 (1996).
29. B. Hammarström, T. Laurell, J. Nilsson, Seed particle-enabled acoustic trapping of bacteria and nanoparticles in continuous flow systems. *Lab Chip* **12**, 4296–4304 (2012).
30. M. Antfolk, P. B. Muller, P. Augustsson, H. Bruus, T. Laurell, Focusing of sub-micrometer particles and bacteria enabled by two-dimensional acoustophoresis. *Lab Chip* **14**, 2791–2799 (2014).
31. Z. Mao, P. Li, M. Wu, H. Bachman, N. Mesyngier, X. Guo, S. Liu, F. Costanzo, T. J. Huang, Enriching nanoparticles *via* acoustofluidics. *ACS Nano* **11**, 603–612 (2017).
32. D. J. Collins, Z. Ma, J. Han, Y. Ai, Continuous micro-vortex-based nanoparticle manipulation *via* focused surface acoustic waves. *Lab Chip* **17**, 91–103 (2017).
33. N. Ashgriz, *Handbook of Atomization and Sprays: Theory and Applications* (Springer Science & Business Media, 2011).
34. R. J. A. Hill, L. Eaves, Nonaxisymmetric shapes of a magnetically levitated and spinning water droplet. *Phys. Rev. Lett.* **101**, 234501 (2008).

35. C. L. Shen, W. J. Xie, B. Wei, Parametrically excited sectorial oscillation of liquid drops floating in ultrasound. *Phys. Rev. E* **81**, 046305 (2010).
36. G. Destgeer, H. Cho, B. H. Ha, J. H. Jung, J. Park, H. J. Sung, Acoustofluidic particle manipulation inside a sessile droplet: Four distinct regimes of particle concentration. *Lab Chip* **16**, 660–667 (2016).
37. Y. Bourquin, A. Syed, J. Reboud, L. C. Ranford-Cartwright, M. P. Barrett, J. M. Cooper, Rare-cell enrichment by a rapid, label-free, ultrasonic isopycnic technique for medical diagnostics. *Angew. Chem. Int. Ed. Engl.* **53**, 5587–5590 (2014).
38. P. R. Rogers, J. R. Friend, L. Y. Yeo, Exploitation of surface acoustic waves to drive size-dependent microparticle concentration within a droplet. *Lab Chip* **10**, 2979–2985 (2010).
39. R. Shilton, M. K. Tan, L. Y. Yeo, J. R. Friend, Particle concentration and mixing in microdrops driven by focused surface acoustic waves. *J. Appl. Phys.* **104**, 014910 (2008).
40. W. Thielicke, E. J. Stamhuis, PIVlab-time-resolved digital particle image velocimetry tool for MATLAB (version: 1.35). *J. Open Res. Softw.* **2**, 10.6084/m9.figshare.1092508 (2014).
41. W. Thielicke, E. J. Stamhuis, PIVlab–towards user-friendly, affordable and accurate digital particle image velocimetry in MATLAB. *J. Open Res. Softw.* **2**, e30 (2014).
42. M. Yáñez-Mó, P. R.-M. Siljander, Z. Andreu, A. B. Zavec, F. E. Borràs, E. I. Buzas, K. Buzas, E. Casal, F. Cappello, J. Carvalho, E. Colás, A. C.-d. Silva, S. Fais, J. M. Falcon-Perez, I. M. Ghobrial, B. Giebel, M. Gimona, M. Graner, I. Gursel, M. Gursel, N. H. H. Heegaard, A. Hendrix, P. Kierulf, K. Kokubun, M. Kosanovic, V. Kralj-Iglic, E.-M. Krämer-Albers, S. Laitinen, C. Lässer, T. Lener, E. Ligeti, A. Linē, G. Lipps, A. Llorente, J. Lötvall, M. Manček-Keber, A. Marcilla, M. Mittelbrunn, I. Nazarenko, E. N. M. N.-'t. Hoen, T. A. Nyman, L. O'Driscoll, M. Olivan, C. Oliveira, É. Pállinger, H. A. Del Portillo, J. Reventós, M. Rigau, E. Rohde, M. Sammar, F. Sánchez-Madrid, N. Santarém, K. Schallmoser, M. S. Ostenfeld, W. Stoorvogel, R. Stukelj, S. G. Van der Grein, M. H. Vasconcelos, M. H. M. Wauben, O. De Wever, Biological properties of extracellular vesicles and their physiological functions. *J. Extracell. vesicles.* **4**, 27066 (2015).
43. P. Zhang, X. Zhou, M. He, Y. Shang, A. L. Tetlow, A. K. Godwin, Y. Zeng, Ultrasensitive detection of circulating exosomes with a 3D-nanopatterned microfluidic chip. *Nat. Biomed. Eng.* **3**, 438–451 (2019).

44. H. Zhang, D. Freitas, H. S. Kim, K. Fabijanic, Z. Li, H. Chen, M. T. Mark, H. Molina, A. B. Martin, L. Bojmar, J. Fang, S. Rampersaud, A. Hoshino, I. Matei, C. M. Kenific, M. Nakajima, A. P. Mutvei, P. Sansone, W. Buehring, H. Wang, J. P. Jimenez, L. Cohen-Gould, N. Paknejad, M. Brendel, K. Manova-Todorova, A. Magalhães, J. A. Ferreira, H. Osório, A. M. Silva, A. Massey, J. R. Cubillos-Ruiz, G. Galletti, P. Giannakakou, A. M. Cuervo, J. Blenis, R. Schwartz, M. S. Brady, H. Peinado, J. Bromberg, H. Matsui, C. A. Reis, D. Lyden, Identification of distinct nanoparticles and subsets of extracellular vesicles by asymmetric flow field-flow fractionation. *Nat. Cell Biol.* **20**, 332–343 (2018).
45. B. H. Wunsch, J. T. Smith, S. M. Gifford, C. Wang, M. Brink, R. L. Bruce, R. H. Austin, G. Stolovitzky, Y. Astier, Nanoscale lateral displacement arrays for the separation of exosomes and colloids down to 20 nm. *Nat. Nanotechnol.* **11**, 936–940 (2016).
46. A. Cheruvanky, H. Zhou, T. Pisitkun, J. B. Kopp, M. A. Knepper, P. S. T. Yuen, R. A. Star, Rapid isolation of urinary exosomal biomarkers using a nanomembrane ultrafiltration concentrator. *Am. J. Physiol. Physiol.* **292**, F1657–F1661 (2007).
47. N. Francois, H. Xia, H. Punzmann, P. W. Fontana, M. Shats, Wave-based liquid-interface metamaterials. *Nat. Commun.* **8**, 14325 (2017).
48. M. Wu, A. Ozcelik, J. Rufo, Z. Wang, R. Fang, T. J. Huang, Acoustofluidic separation of cells and particles. *Microsyst. Nanoeng.* **5**, 32 (2019).
49. T. Salafi, K. K. Zeming, Y. Zhang, Advancements in microfluidics for nanoparticle separation. *Lab Chip* **17**, 11–33 (2017).
50. S. B. Berry, J. J. Lee, J. Berthier, E. Berthier, A. B. Theberge, Open channel droplet-based microfluidics. *bioRxiv*, 436675 (2018).
51. M. Karimi, G. Akdogan, K. H. Dellimore, S. M. Bradshaw, Comparison of different drag coefficient correlations in the CFD modelling of a laboratory-scale Rushton-turbine flotation tank, Proceedings of the Ninth International Conference on CFD in the Minerals and Process Industries, Melbourne, Australia, 10-12 December 2012.
52. F. Yilmaz, M. Y. Gundogdu, Analysis of conventional drag and lift models for multiphase CFD modeling of blood flow. *Korea Aust. Rheol. J.* **21**, 161–173 (2009).
53. J. Lighthill, Acoustic streaming. *J. Sound Vib.* **61**, 391–418 (1978).

54. M. Alghane, B. X. Chen, Y. Q. Fu, Y. Li, J. K. Luo, A. J. Walton, Experimental and numerical investigation of acoustic streaming excited by using a surface acoustic wave device on a 128° YX-$LiNbO_3$ substrate. *J. Micromech. Microeng.* **21**, 15005 (2011).
55. A. B. COMSOL, Comsol multiphysics® v.5.4 www.comsol.com. Stockholm, Sweden. COMSOL AB (2018).
56. J. M. Martel, M. Toner, Inertial focusing in microfluidics. *Annu. Rev. Biomed. Eng.* **16**, 371–396 (2014).
57. L. P. Gor'Kov, On the forces acting on a small particle in an acoustical field in an ideal fluid. *Sov. Phys. Dokl.* **6**, 773 (1962).
58. A. Bobrie, M. Colombo, S. Krumeich, G. Raposo, C. Théry, Diverse subpopulations of vesicles secreted by different intracellular mechanisms are present in exosome preparations obtained by differential ultracentrifugation. *J. Extracell. vesicles.* **1**, 18397 (2012).
59. R. J. Lobb, M. Becker, S. Wen Wen, C. S. F. Wong, A. P. Wiegmans, A. Leimgruber, A. Möller, Optimized exosome isolation protocol for cell culture supernatant and human plasma. *J. Extracell. vesicles.* **4**, 27031 (2015).
60. D. W. Greening, R. Xu, H. Ji, B. J. Tauro, R. J. Simpson, in *Proteomic Profiling* (Springer, 2015), pp. 179–209.
61. H. Shin, C. Han, J. M. Labuz, J. Kim, J. Kim, S. Cho, Y. S. Gho, S. Takayama, J. Park, High-yield isolation of extracellular vesicles using aqueous two-phase system. *Sci. Rep.* **5**, 13103 (2015).
62. S. Mathivanan, J. W. E. Lim, B. J. Tauro, H. Ji, R. L. Moritz, R. J. Simpson, Proteomics analysis of A33 immunoaffinity-purified exosomes released from the human colon tumor cell line LIM1215 reveals a tissue-specific protein signature. *Mol. Cell. Proteomics* **9**, 197–208 (2010).
63. H. Qi, C. Liu, L. Long, Y. Ren, S. Zhang, X. Chang, X. Qian, H. Jia, J. Zhao, J. Sun, X. Hou, X. Yuan, C. Kang, Blood exosomes endowed with magnetic and targeting properties for cancer therapy. *ACS Nano* **10**, 3323–3333 (2016).
64. Z. Zhao, Y. Yang, Y. Zeng, M. He, A microfluidic ExoSearch chip for multiplexed exosome detection towards blood-based ovarian cancer diagnosis. *Lab Chip* **16**, 489–496 (2016).

65. S. S. Kanwar, C. J. Dunlay, D. M. Simeone, S. Nagrath, Microfluidic device (ExoChip) for on-chip isolation, quantification and characterization of circulating exosomes. *Lab Chip* **14**, 1891–1900 (2014).